Journal of Magnetic Resonance **143,** 106–119 (2000)
doi:10.1006/jmre.1999.1994, available online at http://www.idealibrary.com on IDEAL®

The Bloch Equations in High-Gradient Magnetic Resonance Force Microscopy: Theory and Experiment

W. M. Dougherty,*[,1] K. J. Bruland,* S. H. Chao,* J. L. Garbini,* S. E. Jensen,* and J. A. Sidles†

**Department of Mechanical Engineering and †Department of Orthopaedics, University of Washington, Seattle, Washington 98195*

E-mail: dough@lepton.phys.washington.edu

Received July 9, 1999; revised November 29, 1999

We report theory and observations of paramagnetic resonance in a measured field gradient of 44,000 T per meter by the technique of magnetic resonance force microscopy (MRFM). Resonance was induced in a dilute solid solution of diphenylpicrylhydrazyl in polystyrene at 77 and 10 K by an amplitude-modulated microwave field. This modulated the force between resonant sample spins and a micrometer-scale SmCo magnetic tip on a force microscope cantilever. The force signals were typically of order 10 fN, and were detected above a thermal noise floor of 80 aN per root hertz at 10 K, equivalent to a magnetic moment noise of 200 μ_B per root hertz of bandwidth. Resonance saturation was readily observed. Starting with the Bloch equations, we derived simple analytic expressions for the predicted cantilever signal amplitudes and T_1-dependent phase lags, valid at low microwave power levels. For power levels below saturation, the data were in good agreement with the Bloch equation predictions, while above saturation the measured force increased more slowly with power than predicted. Several ESR mechanisms which might lead to non-Bloch dynamics in the MRFM environment are reviewed. Spin-relaxation mechanisms are also reviewed. A detailed description of the experimental apparatus is offered.

Key Words: **MRFM; Bloch; high gradient; DPPH; ESR.**

This article reports the observation of electron spin resonance (ESR) in a dilute polymer solution of a diphenylpicrylhydrazyl (DPPH) at 77 and 10 K. Historically, these systems have been a rich source of novel ESR physics. During the 1950s, ESR measurements in similar systems yielded—after some initial controversy (*11*, *12*)—early insights into mechanisms of cross-relaxation and spectral diffusion. As ESR theory and experimental techniques matured, studies of dilute polymers during the 1980s (*4*, *3*) yielded excellent agreement with theory, and it became reasonable to regard ESR of dilute solid polymer solutions as a reasonably well-understood subject.

The present experiment explores a new regime of solid-phase ESR which—like the ESR experiments of the 1950s—presents novel theoretical and experimental challenges. One challenge is that ESR is observed in the presence of an extremely strong spatial magnetic gradient: $G = 44{,}000$ T per meter, or equivalently 44 μT/nm. The spin density ρ of our 5% polymer solution was such that the mean spin–spin separation was $\rho^{-1/3} = 2.0$ nm; the polarizing field seen by neighboring DPPH molecules thus differed by $\sim G\rho^{-1/3} = 88$ μT. In comparison, the dipole–dipole interaction field between two neighboring spins was $\sim \mu_0 \hbar \gamma_e \rho/(4\pi) = 250$ μT—the same order of magnitude as the gradient differential field. Our data thus provide an experimental look at a novel ESR realm in which field gradient interactions are comparable in strength to dipole–dipole interactions.

A second and related challenge is that spin relaxation in the environment of magnetic resonance force microscopy (MRFM) is poorly understood. Our experiment measured T_1 at 77 K to be 20 μs, in good agreement with the existing literature. But upon decreasing the temperature to 10 K, T_1 was observed to increase only moderately, to 30 μs. What mechanisms might explain the shorter-than-expected T_1? As we will discuss, the ESR literature suggests many different relaxation mechanisms that might plausibly be operating. This situation has ample historical precedent. In their review of ESR relaxation in traditional bulk samples, Orbach and Stapleton (*23*) emphasize that achieving a firm understanding of relaxation mechanisms in ESR spectroscopy required a 40-year struggle. Progress was achieved by a repetitive cycle which typically began with theoretical predictions of slow relaxation rates based on known relaxation mechanisms, followed by experimental measurements of unexpectedly fast relaxation, followed by theoretical recognition of new relaxation mechanisms—at which point the cycle would begin anew. We expect that the study of ESR relaxation in MRFM will continue this historical pattern.

In this article we take the first simple step toward understanding ESR relaxation in the MRFM environment by asking whether Bloch equations *alone* can quantitatively explain the data, entirely in terms of T_1 and T_2, *without* explicitly taking

[1] To whom correspondence should be addressed at Department of Mechanical Engineering, University of Washington, Room 132, Mechanical Engineering Building, Box 352600, Seattle WA 98195-2600. Fax: (206) 616-2318.

1090-7807/00 $35.00

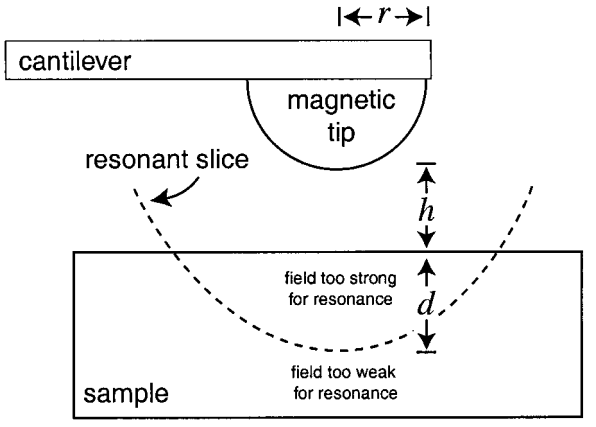

FIG. 1. Basic scheme: The force microscope cantilever detects the modulated spin-gradient force between the magnetic tip and resonant sample spins in the resonant slice. The tip radius is r, the tip–sample separation is h, and the maximal depth of the resonant slice is d. The diagram is not to scale; in our experiment the tip radius r was 2.9 μm and, at 2.0 GHz, the resonant slice was at a fixed distance $d + h = 2.0$ μm from the tip. Note that at a fixed microwave frequency the magnetic resonance condition maintains a fixed tip–slice distance $d + h$, regardless of variation in the tip–sample separation h.

into account spin diffusion and electron–nucleon cross-relaxation mechanisms.

The data reported here were obtained by magnetic resonance force microscopy. This technique combines elements of slice-selective magnetic resonance imaging and force microscopy (*28, 29*), and was originally conceived with the goal of observing spin resonance in individual biological molecules, as a means of directly observing their structure. Since the first MRFM experiment in 1992 (*26, 35*), the spin sensitivity of MRFM devices has increased by a factor of 10^5, with resonant-slice thicknesses now approaching nanometer length scales (*5*). However, the goal of single-spin imaging has not yet been achieved. The shorter-than-expected T_1 we report in this article is currently regarded as the main obstacle to achieving this goal.

A comprehensive series of experiments by Rugar and coworkers at IBM has demonstrated by force detection many of the classical manifestations of magnetic resonance, including spin echoes and nutation (*33*). Several groups have demonstrated MRFM imaging with micrometer-scale resolution (*37, 38, 12*). In addition to electron paramagnetic resonance, ferromagnetic (*36*) and nuclear magnetic resonance (*38, 27*) have been observed with MRFM techniques. Recently, force-detected magnetic resonance has emerged as a new zero-gradient technique for sensitive resonance spectroscopy (*21*).[2]

As in conventional magnetic resonance imaging, MRFM spatial slice selectivity is obtained by the detection of magnetic resonance in a quasi-static magnetic field gradient. In both cases, an applied radiofrequency (RF) field B_1 modulates the magnetization in a thin sample slice that meets the resonance condition $\omega = \gamma B(z)$, where ω is the applied microwave field frequency, γ is the spin gyromagnetic ratio, and $B(z)$ is the polarizing field (induction) at the resonant slice. The basic geometry of MRFM is depicted in Fig. 1.

A schematic diagram of our apparatus appears in Fig. 2. A force microscope cantilever with a micrometer-scale magnetic tip is monitored by a fiber-optic interferometer. Magnetic resonance is induced in a thin sample layer by an applied microwave frequency field, which is pulse-modulated at the cantilever resonance frequency ω_0. The modulated spin-gradient force, typically 10^{-17}–10^{-14} N, excites detectable oscillations of the cantilever, with amplitudes of typically 1–100 pm (picometers). Operation in high vacuum eliminates air-damping of the cantilever. The experiments are performed at cryogenic temperature to increase sample polarization and spin-relaxation time, and to minimize thermal excitation of the cantilever. Thermal excitation of the cantilever is equivalent to a random Langevin force acting on the cantilever, and sets the limit of force sensitivity in MRFM experiments.

Paramagnetic DPPH was diluted to 5% by weight in a solid solution of polystyrene. This system has been well characterized by conventional spin resonance spectroscopy (*31, 14*), and features a spin–lattice relaxation time T_1 which is strongly concentration-dependent.

THEORETICAL RESULTS

Several schemes to modulate sample magnetization by magnetic resonance have been used to successfully excite detectable MRFM signals. These have included adiabatic inversion of the sample spins, and cyclic suppression of the longitudinal magnetization. The experiment described in this article uses the latter technique.

We will calculate the cantilever force signals expected from magnetic resonance in a strong field gradient. Our strategy will be to begin with the Bloch equations and to derive a steady-state nonequilibrium magnetic force acting on the cantilever tip. Then, in a low-power approximation, we will derive the

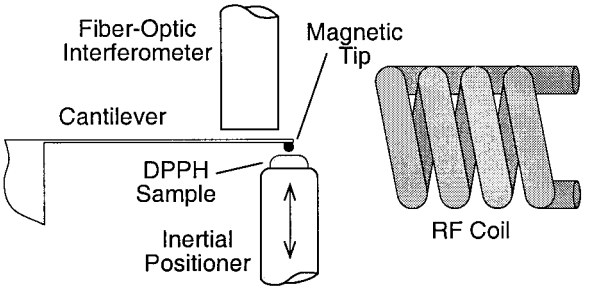

FIG. 2. The heart of the MRFM apparatus, located in a vacuum cryostat. The drawing is roughly to scale—the cantilever is 320 μm long.

[2] Magnetic resonance has been observed indirectly by optical techniques in special single molecules (*18, 17, 34*). These are powerful and useful techniques, but lack the generality of MRFM and conventional magnetic resonance methods that can, in principle, be applied to any NMR or ESR species.

force amplitude and phase response to an amplitude-modulated microwave field. The time dependence of the magnetic pressure can be solved in the Laplace, Fourier, and time domains. All three approaches yield identical results. We will use the Laplace transform method. Finally, as a check on our closed-form results, we will solve the Bloch equations numerically.

We write Bloch equations using the following conventions. Let $\{x, y, z\}$ be a right-handed system of coordinates in a frame rotating with angular frequency ω about the z-axis of the laboratory frame. By convention, the microwave field B_1 is taken to lie along the x-axis of the rotating frame, while the polarizing magnetic field $\mathbf{B}(z) = (B_0 + Gz)\hat{\mathbf{z}}$ and the equilibrium sample polarization $\mathbf{M}_0 = M_0\hat{\mathbf{z}}$ both lie along the z-axis. Here B_0 is a spatially and temporally constant field (induction), and G is the spatial magnetic gradient. We choose the origin of the z-coordinates such that resonance occurs at $z = 0$. Equivalently, the RF angular frequency $\omega = -\gamma B_0$, where $\gamma/(2\pi) = -28.0$ GHz/T is the (negative) gyromagnetic ratio of the electron. The longitudinal and transverse spin-relaxation times are T_1 and T_2, respectively.

The resulting rotating-frame Bloch equations are unusual only in their dependence upon the spatial coordinate z:

$$\frac{\partial M_x}{\partial t} = \gamma M_y G z - \frac{M_x}{T_2} \quad [1]$$

$$\frac{\partial M_y}{\partial t} = \gamma M_z B_1 - \gamma M_x G z - \frac{M_y}{T_2} \quad [2]$$

$$\frac{\partial M_z}{\partial t} = -\gamma M_y B_1 + \frac{M_0 - M_z}{T_1}. \quad [3]$$

We adopt a system of natural units by defining normalizations of the field, time, coordinate, and magnetization terms: $B_1' \equiv \gamma B_1/\omega$, $z' \equiv \gamma G z/\omega$, $t' \equiv \omega t$, and $M_i' \equiv M_i/M_0$. We also introduce relaxation rates $\Gamma_{1,2} \equiv 1/T_{1,2}$ and $\Gamma_{1,2}' \equiv 1/(\omega T_{1,2})$. The use of natural units, denoted by the primes, permits a degree of clarity and economy of notation. Substituting these changes of variables into the Bloch equations and simplifying, we obtain

$$\frac{\partial M_x'}{\partial t'} = -\Gamma_2' M_x' + z' M_y' \quad [4]$$

$$\frac{\partial M_y'}{\partial t'} = -z' M_x' - M_y' \Gamma_2' + B_1' M_z' \quad [5]$$

$$\frac{\partial M_z'}{\partial t'} = -B_1' M_y' - M_z' \Gamma_1' + \Gamma_1'. \quad [6]$$

In an MRFM experiment $B_1'(t)$ is in general an arbitrary periodic function, and (as is well known) the Bloch equations cannot be solved in closed form at this level of generality. To obtain useful results, we pursue the following strategy: (1) we derive a closed-form steady-state solution (assuming B_1 is constant); (2) we derive a closed-form solution that is valid for arbitrary time dependence of $B_1(t)$, but only below saturation ($\gamma^2 T_1 T_2 B_1^2(t) \ll 1$); (3) we combine these two solutions to obtain a simple closed-form approximation that is valid for $B_1(t)$ both large and time-dependent; and (4) we solve the Bloch equations numerically to verify that the closed-form hybrid approximation is accurate.

The Steady-State Solution

In steady state, the derivatives with respect to time are zero, and we solve for M_i',

$$M_x' = \frac{B_1' z'}{z'^2 + \Gamma_2'^2 + B_1'^2 \Gamma_2'/\Gamma_1'} \quad [7]$$

$$M_y' = \frac{B_1' \Gamma_2'}{z'^2 + \Gamma_2'^2 + B_1'^2 \Gamma_2'/\Gamma_1'} \quad [8]$$

$$M_z' = \frac{z'^2 + \Gamma_2'^2}{z'^2 + \Gamma_2'^2 + B_1'^2 \Gamma_2'/\Gamma_1'} \quad [9]$$

where all three equations have the same denominator.

The presence of the sample magnetic moment in the field gradient G creates a force density on the tip $f = -GM_z$. We can compute an effective pressure P (signal force per unit area of resonant slice) by integrating over all z:

$$P = -G \int_{-\infty}^{\infty} dz\, M_z = -\frac{\omega M_0}{\gamma} \int_{-\infty}^{\infty} dz'\, M_z'. \quad [10]$$

We can express the magnetization in terms of the susceptibility χ and the permeability μ_0, $M_0 = \chi\omega/(\mu_0\gamma)$, and define an expression for the normalized pressure, subtracting the static pressure between the sample and the tip:

$$P' \equiv \frac{P\mu_0\gamma^2}{\chi\omega^2} = \int_{-\infty}^{\infty} dz'\, (1 - M_z'). \quad [11]$$

Evaluating the integral yields the steady-state change in magnetic pressure caused by the resonant suppression of M_z,

$$P' = \frac{\pi B_1'^2}{\Gamma_1'(1 + B_1'^2/(\Gamma_2'\Gamma_1'))^{1/2}} \quad [12]$$

or, in SI units,

$$P = \frac{\pi\chi\omega T_1 B_1^2}{\mu_0(1 + \gamma^2 T_1 T_2 B_1^2)^{1/2}}. \quad [13]$$

This solution to the Bloch equations is valid for *any* microwave power B_1^2, *provided* that the power is modulated on timescales long compared to T_1, such that the steady-state approximation is valid.

The most striking feature of [13] is the predicted "knee" in the force–power curve, which occurs when $\gamma^2 T_1 T_2 B_1^2 \sim 1$. Physically, the knee occurs when the RF power is sufficient to saturate the magnetization of the resonant slice at $z = 0$. Observing this predicted knee was one of the main goals of our experiment.

The Low-Power Solution

What happens when the RF power is modulated at an angular frequency ω_0 that is comparable to the spin–lattice relaxation rate? We expect that the time-dependent magnetic pressure $P(t)$ will lag behind the applied power $B_1^2(t)$ with some phase lag θ. In this section we show that this expectation is correct.

The analytic expression we will obtain for the phase lag is simple:

$$\tan\,\theta = \omega_0 T_1. \qquad [14]$$

What is notable (and to us surprising) about [14] is that the phase lag is independent of T_2, and also independent of the modulation scheme (i.e., independent of sinusoidal versus square-wave versus triangular modulation of the RF power). This parameter independence is one of the main theoretical results of this article. From a practical point of view, [14] has the virtue of allowing ready determination of T_1 directly from a measurement of θ.

Equation [14] is most easily derived by solving the Bloch equations [4]–[6] order-by-order in powers of $B_1(t)$. The equations are structured such that the transverse components $\{M_x, M_y\}$ depend only on odd powers of B_1, while M_z depends only on even powers,

$$\begin{aligned} M_z &= 1 + \mathbb{O}(B_1^2) + \mathbb{O}(B_1^4) + \cdots \\ &\quad\searrow\nearrow\quad\searrow\quad\nearrow\quad\searrow \\ \begin{Bmatrix} M_x \\ M_y \end{Bmatrix} &= \mathbb{O}(B_1) + \mathbb{O}(B_1^3) + \cdots. \end{aligned}$$

This structure suggests an iterative solution strategy: start with the lowest-order solution $M_z = 1$, then solve the transverse Bloch equations for $\{M_x, M_y\}$ to $\mathbb{O}(B_1)$, then use this solution to find the $\mathbb{O}(B_1^2)$ corrections to M_z, etc. In numerical calculations the iteration can be continued to any desired order; we present an example of such numerical calculations in a later section of this article. For the present our goal is to carry through the iteration analytically in orders $B_1(t)$ and $B_1^2(t)$.

The $\mathbb{O}(B_1)$ solution for $\{M_x, M_y\}$ is obtained by solving

$$\frac{\partial}{\partial t'}\begin{bmatrix} M_x' \\ M_y' \end{bmatrix} = \begin{bmatrix} -\Gamma_2' & z \\ -z & -\Gamma_2' \end{bmatrix}\begin{bmatrix} M_x' \\ M_y' \end{bmatrix} + \begin{bmatrix} 0 \\ B_1'(t) \end{bmatrix} \qquad [15]$$

whose Laplace transform is

$$\begin{bmatrix} s + \Gamma_2' & -z' \\ z' & s + \Gamma_2' \end{bmatrix}\begin{bmatrix} \tilde{M}_x'(s) \\ \tilde{M}_y'(s) \end{bmatrix} = \begin{bmatrix} 0 \\ \tilde{B}_1'(s) \end{bmatrix} \qquad [16]$$

which we readily solve for $\tilde{M}_y'(s)$

$$\tilde{M}_y'(s) = \frac{(s + \Gamma_2')\tilde{B}_1'(s)}{(s^2 + z'^2 + 2s\Gamma_2' + \Gamma_2'^2)}. \qquad [17]$$

It is not yet clear that we have made much progress, because the inverse Laplace transform of [17] cannot be done in general. However, if we calculate the spatial integral of $\tilde{M}_y$, we obtain the simpler result

$$\int_{-\infty}^{\infty} dz'\ \tilde{M}_y'(s) = \pi\tilde{B}_1'(s). \qquad [18]$$

Taking the inverse Laplace transform of both sides, and reverting to SI units, we obtain the following sum rule:

$$\int_{-\infty}^{\infty} dz\ M_y(z,t) = \frac{\pi\chi\omega}{\mu_0\gamma G}\,B_1(t). \qquad [19]$$

Physically speaking, the spatial integral of $M_y(z,t)$ tracks $B_1(t)$ with no phase lag and with no T_2 dependence.

Combining [3], [11], and [19], we obtain an equation for the time-dependent pressure $P(t)$ to leading order in B_1^2:

$$\left(\frac{\partial}{\partial t} + \frac{1}{T_1}\right)P(t) = \frac{\pi\chi\omega}{\mu_0}\,B_1^2(t). \qquad [20]$$

It is evident that as far as the *net* MRFM force is concerned—and provided that the RF power is below the knee at $B_1^2 \sim 1/(\gamma^2 T_1 T_2)$—the time dependence of the Bloch equations is functionally equivalent to a linear low-pass filter with time constant T_1. The phase lag of the low-pass filter is $\tan^{-1}(\omega_0 T_1)$, the value of T_2 does not enter, and the details of the $B_1^2(t)$ modulation are irrelevant.

Combined Steady-State and Low-Power Solution

A considerable portion of our experimental data is acquired at high RF power, and in this simultaneously high-power and time-dependent regime neither of the solutions in the previous two sections is formally valid. We will therefore combine the results of the previous sections to obtain a closed-form approximate expression for the MRFM signal force. Subsequent numerical calculations will show that, considered as a solution of the Bloch equations, this expression is remarkably accurate

(although looking ahead, the Bloch equations themselves will not accurately describe the high-power ESR/MRFM regime).

In carrying through a calculation of the MRFM force we must take into account both the tip–sample geometry and the microwave modulation waveform. A convenient modulation is a simple on–off rectangular envelope with a fractional-on duty cycle ϵ. The static magnetic field may be modeled as a dipole field produced by a spherical magnetic particle—this appears to be well justified for our magnetic tips (*5*). Refer again to Fig. 1 to identify the magnetic tip radius r, the height h of the tip above the sample surface ($h \ll r$), and the depth d of the resonant surface in the sample ($d \leq r$). For a dipole moment oriented parallel to the sample surface we calculate the rms force amplitude in SI units as

$$\begin{aligned} F_{\text{sig}} &= \sin(\epsilon\pi)/\pi && \Leftarrow \text{RF duty cycle factor} \\ &\times 8\pi(h+r)d/5 && \Leftarrow \text{resonant slice area} \\ &\times P_{\text{sig}}/\sqrt{2} && \Leftarrow \text{rms force per unit area.} \end{aligned} \qquad [21]$$

For the approximate force per unit area P_{sig} we combine the low-power result for the phase lag with the steady-state expression for the force amplitude:

$$\begin{aligned} P_{\text{sig}} &= \frac{1}{(1+(\omega_0 T_1)^2)^{1/2}} && \Leftarrow \begin{cases} \text{power factor} \\ \text{from phase lag} \end{cases} \\ &\times \frac{\pi\chi\omega T_1 B_1^2}{\mu_0(1+\gamma^2 T_1 T_2 B_1^2)^{1/2}} && \Leftarrow \begin{cases} \text{steady state} \\ \text{force magnitude.} \end{cases} \end{aligned} \qquad [22]$$

Note that the gradient G does not appear in the expression for the net MRFM signal force. This reflects a notable scaling feature of MRFM; as the gradient is made stronger, the resonant slice becomes thinner, such that the net signal force per unit area is constant.

High-Order Perturbative Solutions

The main limitation of the approximate expression [21]–[22] is that its derivation provides no guarantee that the predicted high-power scaling $F_{\text{sig}} \propto B_1$ is correct. We need to check these expressions against a more rigorous solution of the Bloch equations.

Given an arbitrary periodic RF modulation $B_1^2(t)$, and assuming $T_2 \ll T_1$ (which is reasonable for our experiments), the Bloch equation prediction for pressure P_{Bloch} can be evaluated to any desired accuracy by the method described in the following paragraphs. We warn the reader that such calculations are "a long run for a short slide," because they yield a final result in close agreement with the simple expression [21]–[22].

We will work with the change in sample magnetization defined by $\delta M_z(z,t) \equiv M_z(z,t) - M_0$. We note that in our experiment $T_2 \sim 20$ ns is by far the shortest timescale of the system, the two other timescales being $T_1 \sim 20$ μs and the inverse modulation time $1/\omega_0 \sim 20$ μs. We therefore set $\partial M_x/\partial t = \partial M_y/\partial t = 0$ in the transverse Bloch equations [1]–[2], which allows us to solve for M_x and M_y algebraically. Physically, we are reasoning that the short T_2 maintains the transverse magnetization in instantaneous equilibrium. The remaining z-axis Bloch equation then takes the form (in SI units)

$$\left(\frac{\partial}{\partial t} + \frac{1}{T_1}\right)\delta M_z(z,t) = -\frac{T_2\gamma^2 B_1^2(t)}{\gamma^2 G^2 T_2^2 z^2 + 1}\,(M_0 + \delta M_z(z,t)). \qquad [23]$$

Our task is to solve this equation for $\delta M_z(z,t)$ and then integrate to obtain the "exact" Bloch prediction for the pressure P_{Bloch}:

$$P_{\text{Bloch}} = -\frac{\omega_0 G}{2\pi}\int_0^{2\pi/\omega_0} dt \int_{-\infty}^{\infty} dz\; e^{i\omega_0 t}\delta M_z(z,t). \qquad [24]$$

Here the time integral projects out the Fourier component of $M_z(z,t)$ that is resonant with the cantilever frequency ω_0.

Our solution method is partly numerical and partly analytic. First, we express $B_1^2(t)$ as the sum of n_h harmonics of the fundamental frequency ω_0. For a square wave with duty cycle ϵ, we have explicitly

$$B_1^2(t) = B_1^2 \sum_{k=-n_h}^{n_h} \frac{\sin(k\pi\epsilon)}{k\pi}\, e^{ik\omega_0}, \qquad [25]$$

where B_1 is the (constant) power-on rotating-frame B-field. Then we solve [23] perturbatively, order-by-order in B_1^2, with each successive order generating $2n_h$ new harmonics. Inserting the resulting expression into [24], we can trivially perform the time integral, which projects out the fundamental Fourier component at frequency ω_0. The remaining z-integral is the sum of terms which can be evaluated in closed form

$$\int_{-\infty}^{\infty} dz\, \frac{B_1^{2m}}{(1+\alpha^2 z^2)^m} = \sqrt{\pi} B_1^{2m}\frac{\Gamma(m-1/2)}{\alpha\Gamma(m)}.$$

One mathematical hurdle remains. The resulting expression for P_{Bloch} is in the general form of a power series in B_1^2, which in principle can be evaluated to any desired order n_B:

$$P_{\text{Bloch}} = \sum_{k=0}^{n_B} a_k (B_1^2)^k. \qquad [26]$$

Here the complex coefficients a_k are evaluated numerically from the experimental parameters $\{\epsilon, T_1, T_2\}$ via [23]–[26]. But in its native form this power series is divergent above the

knee at $\gamma^2 T_1 T_2 B_1^2 \sim 1$, and increasing the order n_B of the expansion does not remove the divergence. The reason is clear from [22]; there is a branch-cut singularity in the analytic B_1^2-plane at $\gamma^2 T_1 T_2 B_1^2 \sim -1$. Padé approximants are a well-known method for dealing with such singularities, and we find that the $\{n_B/2, n_B/2\}$ Padé approximant

$$P_{\text{Bloch}} = \frac{\sum_{k=0}^{n_B/2} b_k (B_1^2)^k}{1 + \sum_{k=1}^{n_B/2} c_k (B_1^2)^k} \qquad [27]$$

exhibits excellent above-knee convergence. The coefficients $\{b_k, c_k\}$ are readily calculated from the $\{a_k\}$ of [27] via standard numerical techniques (*24*).

We numerically compared[3] the approximate value P_{sig} [22] with the "exact" Padé result P_{Bloch} [27] for the MRFM parameters typical of our experiment: $\omega_0/(2\pi) = 7792$ Hz, $T_1 = 20$ μs, $T_2 = 20$ ns, and RF duty cycle $\epsilon = 0.29$. The square-wave RF modulation was approximated using $n_f = 24$ starting Fourier components. The perturbative calculation was carried through to order $n_B = 48$, with the final result for P_{Bloch} expressed as a {24, 24} Padé approximant in B_1^2.

The functions P_{sig} and P_{Bloch} agreed perfectly below the knee—as expected—and were in close agreement above the knee. The main difference was that the knee of P_{Bloch} occurred slightly earlier, such that the above-knee magnitude of P_{Bloch} was reduced by about 25% relative to P_{sig}. The predicted above-knee linear scaling $P \propto B_1$—which turns out to be of great interest for comparison with data—was the same in both cases. Varying the expansion parameters n_f and n_B did not alter the results. We conclude that the simple analytic result [22] for P_{sig} is adequate for interpreting our data.

Final Bloch Equation Predictions

Under the reasonable assumption that T_1 is determined by spin–lattice interactions which are strongly temperature-dependent, the Bloch equations predict four ESR/MRFM phenomena:

(1) at low RF power, signal force $F_{\text{sig}} \propto (B_1)^2$;
(2) a knee in the force–RF power curve at $\gamma^2 T_1 T_2 B_1^2 \sim 1$;
(3) above the knee, force $F \propto B_1$; and
(4) sharply increased signal phase lag at 10 K.

The gist of our experiment is that phenomena (1) and (2) were observed, while (3) and (4) were not. Instead, we observed $F \propto (B_1)^{0.55}$ at high RF power, and we observed a signal phase lag which was unexpectedly small at low temperature.

[3] *Mathematica* Version 3.0, Wolfram Research, Champaign, IL. The Padé calculations were carried through with $MaxPrecision = $MinPrecision = 35 to minimize round-off errors.

TABLE 1
Summary of Experimental Parameters

Cantilever-related parameters		
$\omega_0/(2\pi)$	Resonant frequency	7.792 kHz
k	Spring constant	0.015 N/m
m	Motional mass	6.26 pg
Q	Quality	10,000 at 77 K 25,000 at 10 K
Magnetic tip parameters[a]		
M	Tip magnetization	0.52 T/μ_0
r	Tip radius	2900 nm
$h + d$	Tip–slice separation	2010 nm
Resonant slice parameters[a]		
B_0	Polarizing field	71.4 mT
G	Field gradient	44 μT/nm
h	Tip–sample separation	250 nm at 77 K 1700 nm at 10 K
d	maximal slice depth	1760 nm at 77 K 310 nm at 10 K
$2(\gamma G T_2)^{-1}$	Bloch equation slice thickness (spin diffusion ignored)	13 nm
RF parameters		
ω	RF frequency (2.0 GHz)	$12.6 \times 10^9 \text{s}^{-1}$
ϵ	RF square-wave duty cycle	0.29
Thermal noise		
$(S_f)^{1/2}$	Force noise (one sided spectrum)	361 aN/$\sqrt{\text{Hz}}$ at 77 K 82 aN/$\sqrt{\text{Hz}}$ at 10 K
$(S_\mu)^{1/2}$	Equivalent magnetic noise	892 $\mu_B/\sqrt{\text{Hz}}$ at 77 K 203 $\mu_B/\sqrt{\text{Hz}}$ at 10 K
Sample paramagnetic parameters		
ρ	Spin density	1.34×10^{20} cm^{-3}
$\rho^{-1/3}$	Mean spin spacing	2.0 nm
$\frac{\mu_0}{4\pi}\hbar\gamma\rho$	Mean dipole field	0.25 mT
χ	Sample susceptibility	1.36×10^{-5} at 77 K 10.5×10^{-5} at 10 K
Sample relaxation parameters		
T_1	Sample T_1[b]	19.7 μs at 77 K 30.3 μs at 10 K
T_2	Sample T_2[c]	20 ns
$\frac{\mu_0}{4\pi}\hbar\gamma^2\rho^{1/3}$	Spin diffusion scale	167 μm^2/s

[a] This particular tip is one of those whose parameters were measured in (*5*).
[b] T_1 values inferred from the measured signal phase lag via [14].
[c] T_2 value taken from the literature (*31, 14*).

Experimental Results

The concluding section entitled Description of Experiment provides details of our experiment (see also Table 1), but for many readers the following basic information will suffice:

(1) the ESR frequency was always 2.0 GHz;
(2) the field gradient was always 44,000 T/m;
(3) ESR was observed at two temperatures, 77 and 10 K; and
(4) the microwave field ranged over $0 < B_1 \lesssim 0.1$ mT.

Readers will also need to keep in mind a clear picture of MRFM resonant slice geometry. With reference to Fig. 1, at 77

K the tip–sample separation was set to $h = 250$ nm—a relatively close approach—in order to maximize the area of the resonant slice within the sample. But at 10 K the observed signals at this close approach were so large that they overranged our digital cantilever controller. It was necessary to move the tip farther away, to $h \sim 1700$ nm, to reduce the fraction of the resonant slice within the sample, and thus reduce the excessive signal amplitude.

It is important to appreciate that changing the tip–sample separation h does not alter the geometry of the polarizing B-field or its gradient at the resonant slice, but instead changes the fraction of the resonant slice within the sample, and also the proximity d of the slice to the surface, per Fig. 1.

Fitting the Data

We fit our ESR/MRFM data to a three-parameter curve of the general form

$$F_{\text{sig}} = \frac{\alpha B_1^2}{(1 + (\beta B_1^2)^{2-\nu})^{1/2}}. \qquad [28]$$

Note that for small B_1 we have already built in one of the Bloch equation predictions: $F_{\text{sig}} \propto B_1^2$. This scaling was well satisfied in all our data, and we regard it as a successful prediction of the Bloch equations.

The Bloch predictions for $\{\alpha, \beta, \nu\}$ can be determined by inspection of [21] and [22]:

$$\alpha = \frac{8\pi \sin(\epsilon\pi)}{\mu_o 5\sqrt{2}} \frac{d(r+h)\chi\omega T_1}{(1 + (\omega_0 T_1)^2)^{1/2}}, \qquad [29]$$

$$\beta = \gamma^2 T_1 T_2, \qquad [30]$$

$$\nu = 1. \qquad [31]$$

The parameter ν has a simple graphical interpretation: it is the slope of the logarithmic force–RF power curve above the saturation knee. It is important to appreciate that at present the Bloch prediction $\nu = 1$ is the *only* prediction we can rigorously test by curve fitting. While we can determine by curve fitting the parameter α with reasonable accuracy—it is simply the low-power coefficient of the linear force–power relation—we cannot predict it theoretically with comparable accuracy, mainly because it is difficult to measure the required magnetic tip dimensions $\{r, h, d\}$. The parameter β presents the opposite difficulty; we can theoretically predict β in terms of T_1 (determined from phase lag) and T_2 (determined from the literature), but our curve fitting cannot provide an independent determination of β because (at present) we have no independent measurement of B_1, and hence cannot use the knee condition $(\beta B_1)^2 = 1$ to curve fit β. On the other hand, our present data are fully adequate for testing the Bloch equation prediction $\nu = 1$.

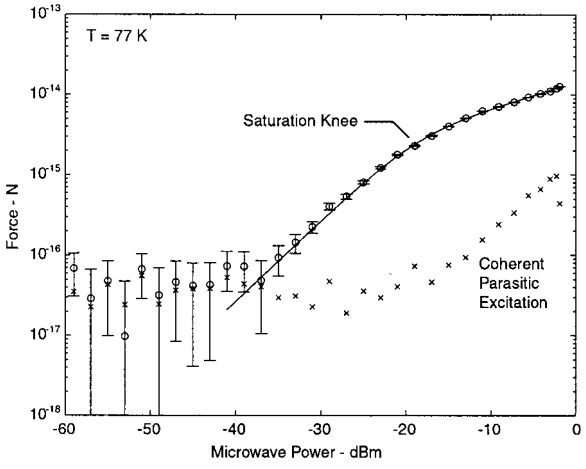

FIG. 3. Observed magnetic resonance force as a function of applied microwave power. The sample was 5% DPPH in polystyrene at 77 K, with a microwave frequency of 2.0 GHz, with a duty cycle of 0.29, amplitude-modulated at the cantilever resonance frequency of 7792 Hz. The magnetic tip–sample separation was 250 nm. Microwave power is measured in decibels referred to 1 mW (dBm), corrected for gain compression, at the microwave synthesizer. The noise floor is the measured Langevin-force equivalent of the thermal (Brownian) motion of the cantilever. The solid line is the curve fit to [29]. Shown also are the phase-coherent parasitic forces induced by the microwave power, independent of magnetic resonance effects.

Description of the Data

Figure 3 shows the measured force acting on the cantilever versus corrected microwave power taken at 77 K. Shown are two curves—one demonstrating magnetic resonance forces, which was taken with the sample near the magnetic tip (height = 250 nm), and the other taken far from the sample, illustrating the residual parasitic background. Errors displayed are statistical, and are calculated from the measurement bandwidth and the force noise power spectral density. The observed noise floor is in good agreement with the noise calculation. The curve fit to [29] yielded $\nu = 0.65$ with systematic error of ± 0.1 estimated by comparing the consistency of several data sets. We remind readers that the the above-knee force–power scaling is $F_{\text{sig}} \propto B_1^{\nu}$; thus our data describe an ESR/MRFM force which, above saturation, increases unexpectedly slowly with increasing RF power.

Data taken at 10 K, Fig. 4, were similar to the higher temperature data, except that for a given microwave power, the resonance forces were much larger. Forces larger than about 50 fN saturated (overranged) the hardware gain configurations for our feedback controller, and so the tip–sample distance for these data was increased. The noise floor is substantially lower at this temperature, as expected. The curve fit to [29] yielded an above-knee slope of $\nu = 0.52$, slightly reduced relative to the 77 K value of 0.65, and only half the Bloch prediction $\nu = 1$.

Figure 5 is a superposition of data taken at 10 and 77 K, with both the forces and the microwave powers normalized to be identical at the knee. Below the knee, the scaling behavior at

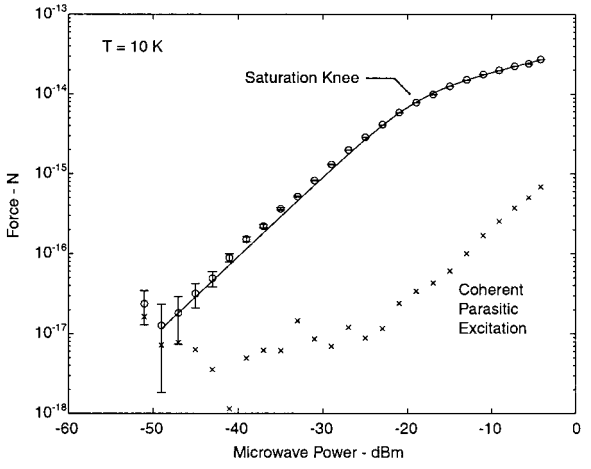

FIG. 4. Resonance force and parasitic signals at 10 K. At this lower temperature, the sample polarization and the resultant forces were much larger for a given tip–sample distance, and saturated our feedback controller at the 77 K tip–sample separation. We moved the sample back to a distance of 1700 nm to operate the controller in a linear mode. The sensitive slice is closer to the surface of the sample, but resonance conditions in the slice—frequency, field, and gradient—were unchanged. The observed noise floor decreases with temperature.

both temperatures is dominated by the B_1^2-term in the numerator in Eq. [13], and consequently we expect the lower portion of the normalized curves to overlap. Above the knee, the curves agree within our estimated errors, which seems to indicate that the unknown saturation mechanism which governs the upper slope is not strongly temperature-dependent.

The phase lag of the cantilever response with respect to the microwave modulation varied with temperature. With liquid nitrogen cooling (77 K) the phase lag was 44°. Equation [14] then yielded a T_1 of 19.7 μs. At 10 K the phase lag was 56°, corresponding to a T_1 of 30.3 μs. In dilute samples prepared as described but measured with conventional spectrometers (*31, 14*), the measured values are $T_1 \simeq 20$ μs at 77 K and $T_1 \simeq 200$ μs at 4 K. Thus our T_1 values at 77 K agree with previous measurements, but the increase in T_1 at 10 K was not as great as the literature lead us to expect. We note that Rugar and co-workers (*33*) have also observed unexpectedly fast relaxation at low temperatures for an entirely different sample material, irradiated silica. The sources of this fast relaxation at cryogenic temperatures are currently unknown.

At higher microwave power levels some coherent parasitic excitation of the cantilever was observed; this parasitic excitation was always much smaller than the MRFM signal. This excitation was measured by performing additional force–power experiments in two ways: (1) by moving the sample well back, >4000 nm, from the magnetic tip, and (2) by substituting a null sample of undoped polystyrene. The forces observed were the same in both cases. As illustrated in Figs. 3 and 4, the parasitic forces were 25–40 dB lower than the magnetic resonance signal, and were below the thermal force–noise floor at lower microwave powers. In addition, the phase response of the parasitic excitation was quite different than the resonance signal, and no temperature dependence was observed. The curve fits for ν included a small correction for this parasitic excitation. Parasitic excitation of the apparatus was minimized by incorporating a short, stiff mechanical path between the cantilever base and the fiber-optic tip, and a small microwave coil volume.

We were able to estimate the value of B_1 at the knee by using a value of T_2 from the literature. Combining T_2 values of 15–30 ns (*31, 14*) with our measured T_1 at 77 K, we find that at the knee $B_1 \simeq (\gamma^2 T_1 T_2)^{-1/2}$ falls in the range 7–10 μT, for a maximum field of order 0.1 mT at full power. In view of the discrepancy between our inferred T_1 value at 10 K and the conventional ESR measurements, this estimate of B_1 should be treated with caution, but is certainly plausible.

DISCUSSION

Our discussion will focus on the two most mysterious aspects of our data. First, what mechanisms might explain the shorter-than-expected T_1 at 10 K? And second, why does the slope of the force–power curve depart from the Bloch equation prediction $F_{sig} \propto B_1$ above saturation, with $F_{sig} \propto B_1^{0.52}$ measured instead at 10 K?

Extrinsic Relaxation Mechanisms

We first consider mechanisms which are *extrinsic* to the DPPH and polystyrene molecules in our sample. Our first clue is that T_1 is not strongly temperature-dependent; such behavior is consistent with dipolar cross-relaxation with a rare but rapidly relaxing species. Al'tshuler and Kozyrev (*1*) review the

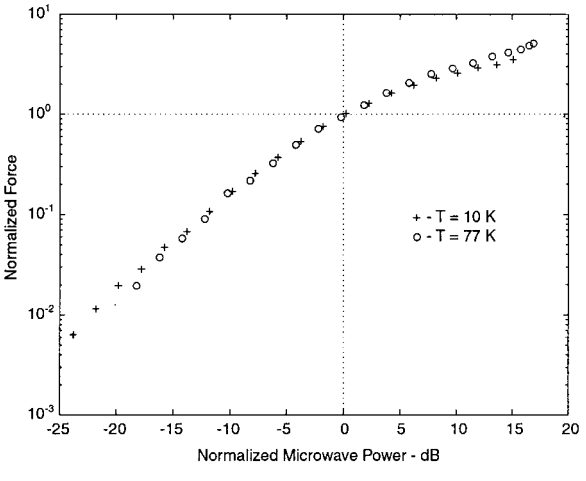

FIG. 5. Universality of the force–microwave power response curves at 77 and 10 K. Data recorded at both temperatures were normalized such that the forces and microwave powers were identical at the knee (crossed dotted lines). Thus, plotted for each curve are force/force(knee) versus microwave power/power(knee). The fact that the curves above the knee lie approximately on top of each other suggests that the saturation mechanisms in play are not strongly temperature-dependent.

extensive literature indicating the O_2 molecule as a well-known culprit in enhancing the relaxation of both pure and dilute organic free radicals. The amount of O_2 in our polymer sample is unknown. Furthermore, it is certainly plausible that O_2 molecules were adsorbed onto the surface of our sample, particularly at 10 K, and we note that the resonant slice was within $d \sim 300$ nm of the sample surface at 10 K (see Table 1). As we will discuss in the following section, this may have been close enough for there to have been appreciable diffusive coupling to occur between the resonant slice and the sample surface.

Less obviously, in MRFM experiments the nearby magnetic tip contains at least four thermal reservoirs which might plausibly couple to spins in the nearby sample. These thermal reservoirs are: (1) paramagnetic spins in the passivating oxide layer of the tip, (2) ferromagnetic spin wave excitations in the tip itself, (3) thermally excited domain wall motions, and (4) thermally excited currents in the conduction band which create an external thermal magnetic noise field.

The conduction band thermal magnetic noise mechanism is particularly intriguing because it contains a natural mechanism yielding (approximately) temperature-independent spin-relaxation rates. According to Varpula and Poutanen's model of thermal magnetic noise (*32*), as recently reviewed by Nenonen *et al.* (*22*), the spectral density of the thermal magnetic field external to a conductor is proportional to $\sigma(T)T$, where T is the temperature and $\sigma(T)$ is the conductivity. To the extent that decreases in temperature are offset by increases in the conductivity of the tip, spin relaxation induced by thermal magnetic noise might be approximately independent of temperature.

If the history of ESR is any guide (*23*), it will be some considerable time before all the extrinsic relaxation mechanisms in MRFM experiments are fully understood. It is plausible that several of the above extrinsic mechanisms were simultaneously active in our experiment, and much additional experimentation may be required to sort them all out.

The present—entirely pragmatic—practice within the MRFM community is to regard these extrinsic relaxation mechanisms as undesired features of an experiment, to be minimized or eliminated if possible by careful engineering design.

Intrinsic Relaxation Mechanisms

Next, we will consider ESR phenomena within an ideal sample of 5% DPPH in polystyrene, and we will ignore all of the extrinsic thermal reservoirs mentioned in the preceding section. We begin by asking, how far does a quantum of DPPH polarization diffuse between RF pulses? For a spin density $\rho \sim 1.3 \times 10^{20}$ cm^{-3}, as in our experiment (see Table 1), the spin diffusion constant D is of order $\mu_0 \hbar \gamma^2 \rho^{1/3}/(4\pi) \sim 170$ μm^2/s. For a cantilever frequency $\omega_0/(2\pi) = 7792$ Hz, the characteristic diffusion distance between successive RF pulses is thus of order $(D/\omega_0)^{1/2} \sim 60$ nm.

Now, in conventional bulk ESR experiments 60 nm is not very far, but in the high-gradient MRFM world it is a relatively large distance. For example, in the field gradient of 44 μT/nm in our experiments it would imply single-pulse spin diffusion across a B-field differential of 2.4 mT. Such cross-gradient electron spin diffusion is, of course, energetically forbidden *unless* there is a compensating adjustment of the dipolar potential energy or a counterflow of dynamical nuclear polarization; Genack and Redfield seem to have been among the first to consider these possibilities (*10*). In contrast, the Bloch equations without diffusion predict a resonant slice thickness $\sim 2/(G\gamma T_2) \simeq 13$ nm, which is substantially thinner than the diffusion length scale. It would be mathematically straightforward to add a spatial diffusion term to [23]; this might explain the non-Bloch behavior we observed in the force–power curves. But until a more complete theory is developed of electron–nucleon dipolar interactions in the strong-gradient MRFM environment, it is hard to know how large the coefficient of such a diffusive term should be.

We are thus led to a concluding question: how do spin diffusion and electron–nucleon dipolar interactions manifest themselves in ESR/MRFM environments? The observation of ENDOR and/or dynamic polarization phenomena, if it could be achieved, might help in clarifying these issues.

CONCLUSIONS

The Bloch equations, solved in a high gradient, are adequate for describing many aspects of the microwave-power scaling behavior of this moderately dilute paramagnetic system. But two aspects of our data are poorly explained. First, T_1 at 10 K is shorter than expected, and second, the measured force–power curves depart quite substantially from the Bloch equation predictions above saturation.

At present it is not known whether these phenomena are best ascribed to extrinsic mechanisms, like O_2 sample contamination or magnetic noise originating in the magnetic tip, versus intrinsic mechanisms, like electron–nucleon dipolar interactions, manifesting themselves in the high-gradient MRFM environment. Only future theoretical and experimental work can settle this question.

DESCRIPTION OF EXPERIMENT

A block diagram of the system appears in Fig. 6. We will discuss each of the subsystems.

Vacuum and Cryogenics

The experiments were performed in a flow cryostat (Janis Research Systems, Modified Model ST400) evacuated by a turbomolecular pump to a pressure of 10^{-6} Torr or lower. The cryostat was bolted to a concrete building support column without additional vibration isolation. Vacuum feedthroughs transmitted the required experimental signals: optical, micro-

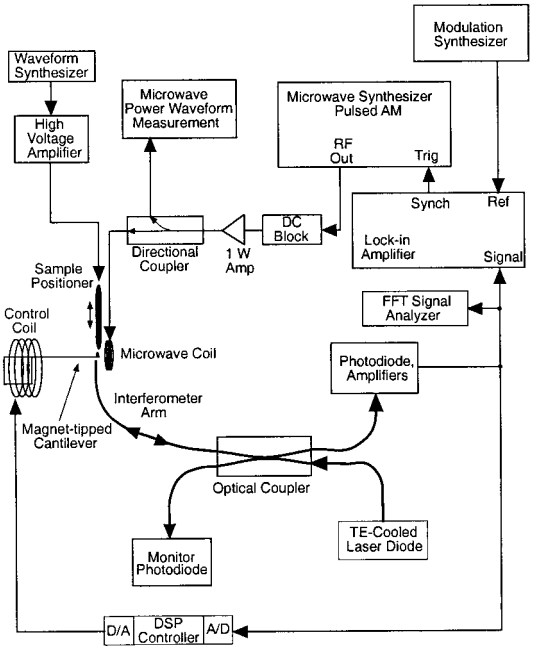

FIG. 6. Apparatus schematic, depicting the magnet-tipped cantilever, fiber-optic interferometer, microwave coil, piezo-actuated sample holder, microwave and detection electronics, and the cantilever-feedback controller.

wave, sample positioning, tip control, and temperature sensing. The MRFM experimental module was mounted to the cryostat cold head, which was cooled by liquid helium or nitrogen conveyed from a Dewar by a flexible vacuum–jacket transfer line. Vibrations caused by flowing and boiling cryogen were observed at high flow rates. These vibrations, "flow noise," can be particularly troublesome with liquid helium, which requires a higher flow rate than LN. Flow noise was largely eliminated by the use of a copper-mesh heat exchange device we devised that attaches to the end of the transfer line. This device lowers the coupling of mechanical vibrations from the boiling turbulence while improving the overall thermal efficiency, allowing for reduced LHe consumption. We have observed that lower stiffness cantilevers isolate the tip from base vibrations.

Cantilever

A commercial force microscope cantilever was used in the present experiment, with a spring constant k of 0.015 N/m. These cantilevers have the shape of an open triangle, 320 μm long, with arms 22 μm wide and 0.6 μm thick (Park Scientific Instruments, Microlever C). The cantilever resonance frequency, $f_0 = \omega_0/2\pi$, was 7792 Hz at room temperature, with a resonant quality Q of 10,000. When cooled to 77 K, the resonance frequency rose approximately 80 Hz, and the Q increased to 25,000. Since each vibration mode of the cantilever is thermally excited with an energy k_BT, this enables a direct verification of the spring constant through the equality $k\langle x^2\rangle/2 = k_BT/2$, where $\langle x^2\rangle$ is the mean squared cantilever amplitude (*15*). The amplitude was measured as a power spectral density (PSD) with units of meters^2 per Hz. A fit of the PSD resonance curve yielded estimates of Q, f_0, and $\langle x^2\rangle$. An IBM–Stanford collaboration has developed soft, high-Q cantilevers specifically for MRFM that have significantly greater intrinsic force sensitivity than the commercial cantilever we used (*30*).

Optics

The position and motion of the cantilever was measured with a single-mode fiber-optic interferometer (*25*). The interferometer has four optical fiber arms joined by a connectorized 90:10% optical coupler (Gould). Where advantageous, connections were made with low-reflection angled (APC) connectors. The end of one fiber arm directs light to the tip of the cantilever nearby, $d \approx 50$ μm. The interference between light reflected by the tip of the cantilever and light reflected by the end of the fiber was the detected signal. A diode laser (Sharp LTO23, pigtail connector, $\lambda = 780$ nm) provided 200 μW of coupled optical power with coherence length ($L \approx 1$ mm) which is short enough to prevent stray interference from connectors. The light was detected by a photodiode amplifier (New Focus Model 2001) and further amplified (Stanford Research Systems Model SR560) with a roll-off corner at 100 kHz. Optimal operation of the interferometer, "fringe-centering," was achieved by tuning the laser wavelength by varying the temperature of the diode using a Peltier thermoelectric cooler (*6*).

Noise Processes

The measurement noise produced by the interferometer–amplifier system had a PSD larger than the shot-noise limit by a factor of about 6. The effective interferometer noise floor expressed in terms of cantilever displacement was 1.6 pm/$\sqrt{\text{Hz}}$, corresponding to an equivalent noise temperature of 0.3 mK for a cantilever physical temperature of 77 K. Consequently, in conditions of low-to-moderate cryogen flow we were able to achieve thermally limited force sensitivity. A useful way of illustrating this is depicted in Fig. 7. We plot the theoretical and measured force noise power spectral densities for a feedback-controlled cantilever—equivalent force–noise PSD measurements were obtained by measuring the displacement power spectrum and accounting for the closed-loop dynamics. The thermal force PSD $S_F = 2kk_BT/(\pi Q f_0)$ (N^2/Hz) (*29*), computed solely from the cantilever properties and temperature, is white and Gaussian to an excellent approximation, and is plotted in units of N/$\sqrt{\text{Hz}}$. Expressed as an equivalent force noise, the measurement noise curve has a minimum at the cantilever resonance frequency f_0, because a given electro-optical signal corresponds to a very small force at that frequency. At frequencies far from resonance, the cantilever is relatively insensitive, and measurement noise dominates. In the presence of excess noise caused by cryogen flow, spurious mechanical resonances, or other sources, the measured noise

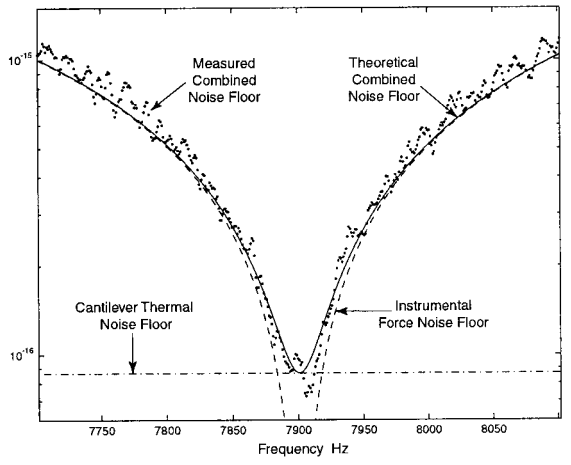

FIG. 7. Comparison of measured versus theoretical equivalent force noise power as a function of frequency. Force noise power spectral densities are plotted here in units of $N/\sqrt{Hz}$. The dot-dashed line is the theoretical thermal noise floor for the cantilever physical temperature, 10 K. The dashed curve is the equivalent force noise floor for combined optics and electronics effects, as derived from measurements. The solid curve is the sum of the noise floors, and the dots are the measured data. The broad width of the curve is a consequence of the feedback control, wherein we commanded an effective resonant Q of 300—the (uncontrolled) natural Q of 25,000 would dictate a resonant width of less than 1 Hz. This plot demonstrates that thermally limited sensitivity can be achieved with a controlled cantilever.

lies above the theoretical curve. We have found this graphical representation to be a valuable diagnostic of day-to-day instrument performance. Furthermore, the expression of all signals and noises in terms of forces and force PSDs greatly eases the reconciliation of theory and experiment.

Probe Head and Sample Positioner

The main body of the apparatus is depicted in Fig. 8. The stainless steel chassis provides a compact base capable of micrometer-scale alignment of the cantilever, the RF (microwave) coil, the sample positioner, and the optical fiber. The chassis was connected to the cryostat cold head by a gold-plated copper base. The sample positioner is actuated by a piezo-electric stick-slip mechanism, consisting of a sapphire cylinder kinematically constrained with magnetic fixation to hardened stainless steel hemispheres. Dissimilar materials, sapphire and stainless steel, were chosen to provide consistent friction in vacuum. Motion occurs only in the axial direction. Actuation is possible in two modes: (1) In linear displacement mode, piezo displacements provide fractional-nanometer-scale sample positioning while maintaining static frictional contact. (2) In stick-slip mode, the cylinder is accelerated forward to high velocity, and then the hemispheres are rapidly retracted backward to break frictional contact. Multiple steps provide actuation over a large range of motion. Between steps the sample holder is operated in the linear displacement mode or passively parked. The stepping waveform (constant acceleration forward, step back; typ. 200 V swing at 10 K) was produced by an arbitrary waveform generator and amplified by a circuit employing a high-voltage operational amplifier (Apex PA-85). Steps were calibrated by moving the sample into contact with the cantilever and determining step displacements from the known interferometer calibration. At a typical operating voltage, steps were 15.5 nm, with an integral nonlinearity of 3.5 nm over a 750-nm travel. When the sample positioner was in motion free from the cantilever, a small, varying interference amplitude was superimposed on the main interferometer signal, created by light transmitted through the nearly transparent cantilever and reflected by the sample. This served as a valuable diagnostic of positioner performance, with a negligible effect on cantilever motion detection.

Microwave Synthesis and Modulation

The resonant microwave field B_1 was produced by a three-turn microcoil 120 μm in diameter. A small coil was chosen to minimize parasitic excitation of the cantilever by the amplitude-modulated microwave field, which has been a serious problem for some MRFM designs. The coil was hand-wound with 30-μm-diameter copper wire and soldered to 1.2-mm-diameter copper 50-Ω semirigid coaxial cable. The coil was designed to have a very high self-resonance frequency and to present an impedance of approximately 50 Ω at our operating frequencies. The impedance was verified by vector network analyzer measurements. Microwave power was transmitted from the vacuum feedthrough via a circuitous path through the cryostat in semirigid 2.2-mm 50-Ω coax, with a stainless steel outer conductor. The material and dimensions were chosen to minimize heat conduction when flowing LHe. The stainless steel coax was connected to the coil coax by SMA connectors.

The modulated microwave signals were generated by a frequency synthesizer (Hewlett Packard Model HP83731A) at power levels from -70 to 0 dBm. These signals were amplified by a 1-W broadband power amplifier (MiniCircuits Model ZVE-8G, 2–8 GHz). Microwave envelope waveforms and power gain compression were measured using a peak power meter with a fast diode sensor (Wavetek Models 8502 and

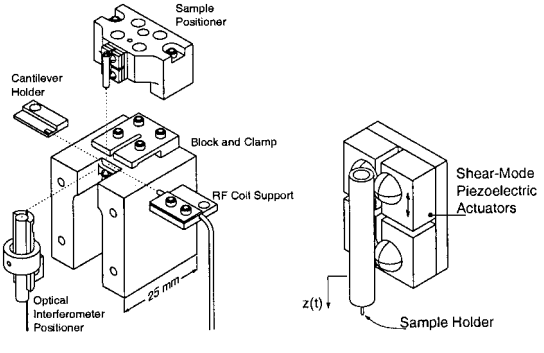

FIG. 8. Exploded view of the chassis with detail of the sample positioner.

16936, respectively). All power levels quoted in this paper are corrected for the measured amplifier gain compression, which was zero at low powers, and up to −3 dB at the highest power, and varied with frequency. The microwave amplitude was pulse modulated with a 28% duty cycle, synchronized with the lock-in reference at the cantilever resonance frequency. A μA current-replica of the modulation envelope appeared at the output of the synthesizer, and was transmitted by the grounds of the microwave system. This potentially troublesome source of parasitic excitation was eliminated by an inside–outside DC block (0.5- to 18.0-GHz passband, Narda Model 4563) inserted between the synthesizer and the amplifier. The synthesizer, amplifier, and vacuum feedthrough were connected by high-performance microwave cables. A directional coupler minimized power return to the amplifier. At microwave frequencies, the lumped cable–feedthrough–coax–coil system presented the amplifier with a frequency-dependent complex impedence, and the power throughput varied significantly with frequency and temperature. The microwave attenuation from the amplifier to the microcoil connector on the stainless steel coax varied with frequency from 12 to 23 dB, as measured at room temperature.

The geometry of the B_1-field was verified by mounting two identical microcoils on micrometer stages with their axes collinear. The coil-to-coil microwave transmission was measured as a function of coil separation using the Wavetek detector. The power–distance curves and inferred dipole dimensions were in good agreement with a dipole–dipole model for these coils. The transmitted power amplitude was in general agreement with theory but could not reliably serve to measure the absolute magnetic field amplitude because of unknown but probably significant impedence mismatches in the test setup. However, from throughput measurements and an electromagnetic model of the coil, we estimated that the maximum B_1 at the sample was of order 0.1 mT, which is consistent with the value inferred from the knee data.

Detection Electronics

All of the major instruments were connected by a GPIB (IEEE-488) interface and controlled by National Instruments LabView software. The software executes experimental protocols automatically. The primary signal detection instrument was a dual-channel DSP lock-in amplifier (Stanford Research Systems SRS 830). A lock-in time constant of 3 s was used, and in-phase and quadrature signal amplitudes were sampled by GPIB at 1.36 Hz and separately averaged for many samples to obtain narrow detection bandwidths with satisfactory lock-in settling times. An FFT dynamic signal analyzer (HP35665A) was essential for measuring the cantilever resonant frequency and quality, and as a general calibration and diagnostic tool.

Control

A critical element of this experiment was the active feedback control of the cantilever dynamics through a magnetic torque on the tip. Feedback accomplishes three goals which greatly enhance the practical effectiveness of soft, high-Q cantilevers (*8*). Optimal feedback (1) broadens the cantilever response bandwidth, (2) reduces the cantilever damping time, and (3) lowers the thermal vibration amplitude. It has been shown in formal optimal control theory and experiment that feedback can accomplish these goals without paying a signal-to-noise-ratio penalty (*9, 7*). The first goal is the most important in the present experiment because the uncontrolled cantilever bandwidth is very narrow and the resonant frequency is subject to change. The frequency changes with tip–sample distance because of tip–sample electrostatic forces, which may be attractive or repulsive, and the attractive van der Waals (Casimir) force (*16, 20, 19*). At close approach, the van der Waals force dominates and tends to counterbalance the spring restoring force, lowering the resonance frequency by as much as several hundred hertz. This frequency is subject to drift in the course of an experiment because of small temperature-related variations of the tip–sample distance in this steep van der Waals-force gradient, and hence a broader resonance is advantageous.

The interferometer signal gave a dynamic measurement of the cantilever tip position. Feedback actuation was provided by a variable magnetic field from a current–loop control coil, producing a variable torque on the magnetic tip. The magnetic torque, τ, coupled to the cantilever of length l, created an effective actuation force acting on the cantilever tip, $F_C \propto \tau/l$. The control coil had three turns, 1.5 mm in diameter, and was wound around the base of the cantilever, oriented with the coil axis parallel to the length of the cantilever. Co-location of the tip position measurement and the control force is desirable for control analysis and stability.

The control algorithm was implemented using a digital signal processor with a 12-bit analog input–output interface.[4] The 10-megasample-per-second digital input stream was decimated to an effective sampling frequency of 500 kHz. The DSP input–output conversion and processing latency of 1.1 μs, in combination with the 2.0-μs output update period (zero-order hold), produced an effective processing delay of 2.1 μs. The analog output provided the control voltage signal, which was converted to a control current by a Howland current source. The dynamic signal analyzer measured the frequency of the freely oscillating cantilever. That information, combined with estimates of thermal and measurement noise, the actual Q, optical, electronic and mechanical transfer functions, and the desired effective Q, was used to compute the coefficients of the algorithm, which is an infinite impulse response filter. When desired, new control coefficients were calculated and loaded automatically if conditions changed during the course of an experiment. Given a cantilever with an uncontrolled natural Q of 25,000, a resonant width of 0.31 Hz, a damping time of 505

[4] Blacktip ISA-bus 40-MHz SHARC processor DSP Board, slightly modified by manufacturer to minimize I/O latency; Bitsi Arrow I/O mezzanine; Bittware Research Systems, Concord, NH.

ms, and a thermal amplitude of 0.27 nm at 77 K, we obtain typical controlled values of 300, 26.3 Hz, 6.1 ms, and 0.036 nm, respectively (*8*).

Sample, Null Sample, and Magnetic Tip

A dilute sample was prepared as a solid solution of diphenylpicrylhydrazyl in polystyrene (5:95% by weight), using benzene as a solvent.[5] The solvent was allowed to evaporate, and a thin cut section of the sample material was glued to the glass-fiber tip of the sample holder. Pure crystalline DPPH has a very high spin density—the estimated spin density of our diluted sample was 1.5×10^{26} spins/m^3. A null sample was prepared in a similar fashion, without DPPH.

The magnetic tip was prepared by selecting a small particle of samarium cobalt magnet and bonding it to the tip of the cantilever[6] using a microscope and micromanipulator. The particle was magnetized by placing the mounted tip in the bore of a 9-T NMR spectrometer magnet. The magnetic tip was the sole source of field and field gradient in this experiment. The tip used in the present experiment was one of those described in (*5*). As described, the field profile near the tip was found to be consistent with that of a dipole produced by a sphere of radius 2.9 μm with a magnetization of 0.54 T/μ_0, and these parameters were in accord with independent estimates from optical measurement and magnetic actuation responsivity.

At an applied RF field of 2.0 GHz, the resonant slice was observed to first intersect with the sample at a tip–sample separation of $h + d = 2000$ nm (see Fig. 1). The gradient of 44 μT/nm predicted by the dipole model agreed well with the gradient measured directly by varying the applied RF frequency and observing the change in the height of first intersection of the resonant slice.

A magnetically hard material was chosen for a high remnant field and to minimize magnetic fluctuations which may tend to relax sample spins. We prefer SmCo to NdFeB magnets because the latter undergo an undesirable magnetic phase change at approximately 135 K (*13*).

Protocol of Experiment

Cryogen flow was adjusted to the lowest flow possible to obtain stable desired temperatures, 77 or 10 K. The position of the sample relative to the cantilever was adjusted to a known position, near (250 or 1700 nm), or far, >4000 nm. The voltage-displacement calibration of the interferometer was measured, as were the amplifier gains. The current-displacement calibration of the magnetic tip actuation was measured, and the uncontrolled natural Q of the cantilever was determined. These data, and the desired effective Q, were used to compute the coefficients of the control algorithm and were downloaded to the DSP. The modulated microwave power was turned on and adjusted in 3-dB steps. The cantilever in-phase and quadrature amplitudes at each power level were measured by the lock-in amplifier, recorded periodically, and vector averaged.

[5] 1,1-Diphenyl-2-picrylhydrazil, Sigma Product Number D9132, and polystyrene, Aldrich Product Number 18,242-7, Sigma–Aldrich Corp., St. Louis, MO 63178.

[6] Type C110 $SmCo_5$ powder, Arnold Engineering, Marengo, IL 60152, bonded with Tempfix adhesive, Electron Microscopy Sciences, Fort Washington, PA 19034.

ACKNOWLEDGMENTS

The authors gratefully acknowledge the support of the National Science Foundation, the National Institutes of Health, the Army Research Office, and the Bristol–Meyers/Zimmer Orthopaedic Research and Education Foundation. We also appreciate the many helpful comments and reviews by our University of Washington colleagues and others.

REFERENCES

1. S. A. Al'tshuler and B. M. Kozyrev, "Electron Paramagnetic Resonance," Academic Press, San Diego (1964).
2. N. Bloembergen, S. Shapiro, P. S. Pershan, and J. O. Artman, Cross-relaxation in spin systems, *Phys. Rev.* **114**(2), 445–459 (1959).
3. R. Bosciano, F. M. Gelardi, and R. N. Mantegna, The experimental detection of spectral diffusion by the saturation transient method, *J. Magn. Reson.* **70,** 262–269 (1986).
4. R. Bosciano, F. M. Gelardi, and R. N. Mantegna, Spectral diffusion and saturation kinetics in inhomogeneous systems, *J. Magn. Reson.* **70,** 251–261 (1986).
5. K. J. Bruland, W. M. Dougherty, J. L. Garbini, S. H. Chao, and J. A. Sidles, Force-detected magnetic resonance in a field gradient of 250,000 tesla per meter, *Appl. Phys. Lett.* **73,** 1959–1964 (1998).
6. K. J. Bruland, J. L. Garbini, W. M. Dougherty, S. H. Chao, S. E. Jensen, and J. A. Sidles, Thermal tuning of a fiber-optic interferometer for maximum sensitivity, *Appl. Phys. Lett.* **70,** 3542–3544 (1999).
7. K. J. Bruland, J. L. Garbini, W. M. Dougherty, and J. A. Sidles, Optimal control of force microscope cantilevers. II. Magnetic coupling implementation, *J. Appl. Phys.* **80**(4), 1959–1964 (1996).
8. K. J. Bruland, J. L. Garbini, W. M. Dougherty, and J. A. Sidles, Optimal control of ultrasoft cantilevers for force microscopy, *J. Appl. Phys.* **83,** 3972–3977 (1998).
9. J. L. Garbini, K. J. Bruland, W. M. Dougherty, and J. A. Sidles, Optimal control of force microscope cantilevers. I. Controller design, *J. Appl. Phys.* **80**(4), 1951–1958 (1996).
10. A. Z. Genack and A. G. Redfield, Nuclear spin diffusion and its thermodynamic quenching in the field gradients of a type-ii superconductor, *Phys. Rev. Lett.* **31**(19), 1204–1207 (1973).
11. J. A. Giordmaine, L. E. Alsop, F. R. Nash, and C. H. Townes, Paramagnetic relaxation at very low temperatures, *Phys. Rev.* **109**(2), 302–311 (1957).
12. P. C. Hammel, Z. Zhang, G. J. Moore, and M. L. Roukes, Subsurface imaging with the magnetic resonance force microscope, *J. Low Temp. Phys.* **101**(1), 59–69 (1995).
13. S. Heisz and G. Hilscer, The origin of graduated demagnetization curves of Nd-Fe-B magnets, *J. Magn. Mater.* **67,** 20–28 (1987).
14. G. Höcherl and H. C. Wolf, Zur konzentrationsabhängigkeit der elektronspin-relaxationszeiten von diphenyl-picryl-hydrazyl in fester phase, *Z. Phys.* **183,** 341–351 (1964).

15. J. L. Hutter and J. Bechhoefer, Calibration of atomic-force microscope tips, *Rev. Sci. Instrum.* **64**(7), 1868–1873 (1993).
16. J. L. Hutter and J. Bechhoefer, Measurement and manipulation of van der Waals forces in atomic force microscopy, *J. Vacuum Sci. Technol. B* **12**(3), 2251–2253 (1994).
17. J. Kohler, J. A. J. M. Disselhorst, M. C. J. M. Donckers, E. J. J. Groenen, J. Schmidt, and W. E. Moerner, Magnetic resonance of a single molecular spin, *Nature* **363,** 242–244 (1993).
18. J. Kohler, A. C. J. Brouwerand, E. J. J. Groenen, and J. Schmidt, Single molecule electron paramagnetic resonance spectroscopy: Hyperfine splitting, *Science* **268,** 1457–1460 (1995).
19. D. Kupiszewska, Casimir effect in absorbing media, *Phys. Rev. A* **46**(5), 2286–2294 (1992).
20. L. D. Landau, E. M. Lifshitz, and L. P. Pitaevskii, "Statistical Physics. Part 2. Theory of the Condensed State (Course of Theoretical Physics)," 3rd ed., Vol. 9, Butterworth–Heineman, Oxford (1980).
21. G. M. Leskowitz, L. A. Madsen, and D. P. Weitekamp, Force-detected magnetic resonance without field gradients, *Solid State Nucl. Magn. Reson.* **11,** 73–86 (1998).
22. J. Nenonen, J. Montonen, and T. Katila, Thermal noise in biomagnetic measurements, *Rev. Sci. Instrum.* **67,** 2397–2405 (1996).
23. R. Orbach and H. J. Stapleton, Electron spin–lattice relaxation, *in* "Electron Paramagnetic Resonance" (S. Geschwind, Ed.), pp. 121–216, Plenum Press, New York (1972).
24. W. H. Press, B. P. Flannery, S. A. Teukolsky, and W. T. Vetterling, "Numerical Recipes: The Art of Scientific Computing," 2nd ed., Cambridge Univ. Press, Cambridge, Cambridge, UK (1994).
25. D. Rugar, H. J. Mamin, and P. Guethner, Improved fiber-optic interferometer for atomic force microscopy, *Appl. Phys. Lett.* **55**(25), 2588–2590 (1989).
26. D. Rugar, C. S. Yannoni, and J. A. Sidles, Mechanical detection of magnetic resonance, *Nature* **360**(6404), 563–566 (1992).
27. A. Schaff and W. S. Veeman, Mechanically detected nuclear magnetic resonance image of a multilayer system at normal pressure, *Appl. Phys. Lett.* **70,** 73–86 (1997).
28. J. A. Sidles, Noninductive detection of single-proton magnetic resonance, *Appl. Phys. Lett.* **58**(24), 2854–2856 (1991).
29. J. A. Sidles, J. L. Garbini, K. J. Bruland, D. Rugar, O. Züger, S. Hoen, and C. S. Yannoni, Magnetic resonance force microscopy, *Rev. Mod. Phys.* **67**(1), 249–265 (1995).
30. T. D. Stowe, K. Yasumura, T. W. Kenny, D. Botkin, K. Wago, and D. Rugar, Attonewton force detection using ultrathin silicon cantilevers, *Appl. Phys. Lett.* **71,** 288–290 (1997).
31. J. Turkevich, J. Soria, and M. Che, Localization of energy in organic molecules as revealed by dynamic nuclear polarization in diphenylpicrlhydrazyl in polystyrene, *J. Chem. Phys.* **56,** 1463–1466 (1972).
32. T. Varpula and T. Poutanen, Magnetic field fluctuations arising from thermal motion of electric charge in conductors, *J. Appl. Phys.* **55,** 4015–4021 (1984).
33. K. Wago, D. Botkin, C. S. Yannoni, and D. Rugar, Force-detected electron-spin resonance: Adiabatic inversion, nutation, and spin echo, *Phys. Rev. B: Condens. Matter* **57,** 1108–1114 (1998).
34. J. Wrachtrup, C. von Borczyskowski, J. Bernardand, M. Orrit, and R. Brown, Optical detection of magnetic resonance in a single molecule, *Nature* **263,** 244–245 (1993).
35. C. S. Yannoni, O. Züger, J. A. Sidles, and D. Rugar, Magnetic resonance force microscopy, *in* "Encyclopedia for Magnetic Resonance" (D. M. Grant and R. K. Harris, Eds.), Wiley, Sussex (1995).
36. Z. Zhang, P. C. Hammel, and P. E. Wigen, Observation of ferromagnetic resonance in a microscopic sample using magnetic resonance force microscopy, *Appl. Phys. Lett.* **68**(14), 2005–2507 (1996).
37. O. Zügar and D. Rugar, Magnetic resonance detection and imaging using force microscope techniques, *J. Appl. Phys.* **75**(10), 6211–6216 (1994).
38. O. Züger, S. T. Hoen, C. S. Yannoni, and D. Rugar, Three-dimensional imaging with a nuclear magnetic resonance force microscope, *J. Appl. Phys.* **79**(4), 1881–1884 (1996).